Asia Pacific Science Press

Journal of Advances in Engineering and Technology
ISSN(O): 3005-7507
ISSN(P): 3005-7493
https://doi.org/10.62177/jaet.v1i2.47

Aerodynamic Optimization and CFD Simulation of Flying Cars

Yipan Wang*

YK Pao School, Shanghai, 200042, China

**Corresponding author:* Yipan Wang

Abstract: With the acceleration of global urbanization, the number of motor vehicles is increasing rapidly, and while this growth has improved people's mobility, it has also brought serious air pollution problems. In this study, we discuss the three main methods of aerodynamics research: experimental simulation, theoretical analysis and numerical calculation, and study the aerodynamic characteristics of the support and propulsion system of the flying car through CFD simulation.

Keywords: Flying Cars; Computational Fluid Dynamics; Resistance Optimization; Numerical Simulation; SST k-ω Turbulence Model

Published: Sept 06, 2024

1. Introduction

As urbanization continues, more and more people are using cars and other motor vehicles as their main method of transportation. According to CEIC, the number of motor vehicle sales in the US had enjoyed a steady monthly growth rate of 1.7% from January 1977 to June 2024[1]. Globally, there are around 2.2 billion registered motor vehicles[2]. However, this proliferation in motor vehicles did not come without its costs[3].The main negative impact of the large number of motor vehicles is the air pollution caused by tailpipe emissions. Tailpipe emissions pollute the environment in two main ways[4]: greenhouse gases from the internal combustion engine and fine particulates from the internal combustion engine. Greenhouse gases cause global warming by inducing the enhanced greenhouse effect[5], whereas fine particulates directly impact human health by increasing the likelihood of respiratory diseases. Transportation related air pollution (TRAP) was found to be the cause of 53% of PM10 and 66% of PM2.5 in European cities. Moreover, fine particulate pollution and ozone pollution from motor vehicles was found to cause 385,000 premature deaths globally by Anenberg et al. (2019).To solve these problems, several solutions had been proposed. Most notably, the concept of a low flying car had been proposed and explored as a potential solution to the problems posed by traditional motor vehicles. Flying cars and vehicles can make the most of the lower airspace, which is currently unused[6], effectively reducing traffic congestion on the ground[7]. Throughout history, many prototypes and concepts revolving around flying cars had been developed by various researchers and companies[8], but currently, there are no models that are commercially available.

2. Aerodynamic Numerical Calculation Principles

2.1 Aerodynamic Research Methods

In the research of aerodynamics, there are three main methods: experimental simulations, theoretical analysis, and numerical

calculations using computational fluid dynamics[9].

(1) Experimental simulations

Many modern experimental simulations for aerodynamic research happen within a wind tunnel[10]. A wind tunnel is a facility where a section is sealed off from the outside to minimize the effect of outside airflow on the airflow inside the testing section. The wind tunnels can be categorized into 4 main types based on the speed of the airflow inside. Subsonic wind tunnels refer to wind tunnels that have wind speeds under 0.8 Mach, transonic wind tunnels refer to wind tunnels that have wind speeds between 0.8 and 1.2 Mach, supersonic wind tunnels refer to wind tunnels that have wind speeds between 1.2 and 5.0 Mach, and hypersonic wind tunnels can have wind speeds over 5.0 Mach.

In a wind tunnel, researchers usually use models of the real object to simulate airflow around it. Wind tunnels are often not very large in size due to the high cost of maintenance and high cost of energy to maintain airflow at high speeds. However, researchers can freely adjust the placement and angle of the model, which can simulate airflow behavior in different scenarios. Researchers can also use markers, such as paint, oil, or smoke, to visualize the airflow above the model, gaining insights on its aerodynamic behavior.

(2) Theoretical analysis

A lot of research around aerodynamics revolves around theoretical analysis[11]. There are a lot of theories in the field of aerodynamics, including but not limited to theory of airfoils and theory of control surfaces, theory of boundary layers, theory of turbulent flow, theory of transonic and hypersonic flow, theory of aircraft performance etc.

One of the most important theories within aerodynamics is the theory of boundary layers proposed by Ludwig Prandtl. The basic assumption of this theory is: flow can be divided into two basic parts. The first part is close to the surface of the object, in which the flow will be affected by viscosity. That layer is named the boundary layer. The drag and flow characteristics of the airflow in the boundary layer can be solved using the Navier-Stokes equations. The flow outside of that layer is assumed to be unaffected by viscosity, hence, it can be solved using Euler's equations.

(3) Computational Fluid Dynamics (CFD)

Computational Fluid Dynamics analysis became popular in modern times in the research of aerodynamics. CFD analysis relies on computers to simulate fluid flow over an object. Meanwhile, the computer will also solve the corresponding Navier-Stokes equations and Euler's equations that are specific to the case. After the calculations, the fluid flow can be visualized using pressure contours or vector images of the velocity of the fluid flow around the object.

CFD analysis is a very cost effect method of conducting aerodynamic research. Meanwhile, utilizing the performance and power of computers can greatly speed up calculations, making research more efficient. Researchers often pair CFD analysis with wind tunnel testing to gain a complete understanding of flow behavior[12].

2.2 Mathematical Models in Computational Fluid Dynamics Analysis

(1) Inviscid flow

Inviscid flow can be modelled using Euler's equations.

For any flow, three principles must be followed: mass is conserved, force equals mass times acceleration (Newton's second law), and energy is conserved (Anderson).

The three principles could be represented by the following partial differential equations:

Continuity equation (Mass conservation):

$$\frac{\partial \rho}{\partial t} + \nabla \cdot (\rho V) = 0$$

Momentum equations (Force equals mass times acceleration):

$$\rho \frac{Du}{Dt} = -\frac{\partial p}{\partial x}$$

$$\rho \frac{Dv}{Dt} = -\frac{\partial p}{\partial y}$$

$$\rho \frac{Dw}{Dt} = -\frac{\partial p}{\partial z}$$

Energy equation:

$$\rho \frac{D(e + V^2/2)}{Dt} = \rho \dot{q} - \nabla \cdot (pV)$$

Where:

$$\frac{D}{Dt} \equiv \frac{\partial}{\partial t} + \nabla \cdot (pV)$$

(2) Viscous flow

Viscous flow, which includes laminar and turbulent flows, can be modelled by Navier-Stokes equations[13].

Viscous flows are fluid flows where it is affected by heat conduction and friction. For viscous flows, the same principles still apply, where mass is conserved, force equals mass times acceleration, and energy is conserved (Anderson).

Continuity equation (Mass conserved):

$$\frac{\partial \rho}{\partial t} + \nabla \cdot (\rho V) = 0$$

x-momentum equation:

$$\rho \frac{Du}{Dt} = -\frac{\partial p}{\partial x} + \frac{\partial \tau_{xx}}{\partial x} + \frac{\partial \tau_{yx}}{\partial y} + \frac{\partial \tau_{zx}}{\partial z}$$

y-momentum equation:

$$\rho \frac{Dv}{Dt} = -\frac{\partial p}{\partial y} + \frac{\partial \tau_{xy}}{\partial x} + \frac{\partial \tau_{yy}}{\partial y} + \frac{\partial \tau_{zy}}{\partial z}$$

z-momentum equation:

$$\rho \frac{Dw}{Dt} = -\frac{\partial p}{\partial z} + \frac{\partial \tau_{xz}}{\partial x} + \frac{\partial \tau_{yz}}{\partial y} + \frac{\partial \tau_{zz}}{\partial z}$$

Energy equation:

$$\rho \frac{D\left(e + \frac{V^2}{2}\right)}{Dt} = \rho \dot{q} + \frac{\partial}{\partial x}\left(k \frac{\partial T}{\partial x}\right) + \frac{\partial}{\partial y}\left(k \frac{\partial T}{\partial y}\right) + \frac{\partial}{\partial z}\left(k \frac{\partial T}{\partial z}\right) - \nabla \cdot (pV) + \frac{\partial (u\tau_{xx})}{\partial x} + \frac{\partial \left(u\tau_{yx}\right)}{\partial y} + \frac{\partial (u\tau_{zx})}{\partial z} + \frac{\partial (v\tau_{xy})}{\partial x} + \frac{\partial (v\tau_{yy})}{\partial y} + \frac{\partial (v\tau_{zy})}{\partial z} + \frac{\partial (w\tau_{xz})}{\partial x} + \frac{\partial (w\tau_{yz})}{\partial y} + \frac{\partial (w\tau_{zz})}{\partial z}$$

Where:

$$\tau_{xy} = \tau_{yx} = \mu\left(\frac{\partial v}{\partial x} + \frac{\partial u}{\partial y}\right)$$

$$\tau_{yz} = \tau_{zy} = \mu(\frac{\partial w}{\partial y} + \frac{\partial v}{\partial z})$$

$$\tau_{zx} = \tau_{xz} = \mu(\frac{\partial u}{\partial z} + \frac{\partial w}{\partial x})$$

$$\tau_{xx} = \lambda(\nabla \cdot V) + 2\mu\frac{\partial u}{\partial x}$$

$$\tau_{yy} = \lambda(\nabla \cdot V) + 2\mu\frac{\partial v}{\partial y}.$$

2.3 Mathematical Model Chosen for This Project

In the simulation software chosen for this project ANSYS Fluent, the finite volume method (FVM) is utilized in the solver[14].To be more specific, ANSYS Fluent utilizes cell-centered finite volumes, which means that centers of the mesh elements store values instead of the vertices.

ANSYS Fluent Solver solves for the characteristics of fluid flow using the numerical model of the Reynolds-Averaged Navier-Stokes equations (RANS). RANS are a set of equations that offer a good approximation of time-averaged solutions to the Navier-Stokes equations[15], which could be very difficult to solve (Qu et al.).

RANS equations (Qu et al.):

$$\frac{\partial u_i}{\partial t} + u_j\frac{\partial u_i}{\partial x_j} = -\frac{1}{\rho}\frac{\partial p_{rgh}}{\partial x_i} + \upsilon\frac{\partial^2 u_i}{\partial x_j^2} - \frac{\partial \overline{u_i' u_j'}}{\partial x_j}$$

$$\frac{\partial u_i}{\partial x_i} = 0$$

In this set of equations, p_{rgh} is the excess pressure apart from the original hydrostatic pressure, u_i represent the fluid velocity expressed in Cartesian components, fluid density is represented by ρ, and υ represents the kinematic viscosity.

The extra term $\overline{u_i' u_j'}$ represents the Reynold's stress component, which needs to be closed to solve the Reynolds-averaged Navier-Stokes equations (Qu et al.). The methods to close the Reynold's stress component include approximating the value of it using first order models or approximating the unknowns in the stress component's transport equations using second order models. First order models to close the Reynold's stress component include: k-epsilon model, k-omega model, SST k-omega model, realizable k-epsilon model etc.

For this essay, the turbulence model of SST k-omega was chosen, as it could provide the best modelling of fluid flow[16].The SST k-omega model combines the k-epsilon model and the k-omega model, where the k-epsilon model is used to predict turbulence in the far-field region and the k-omega model is used to predict turbulence in the near wall regions. This prevents k-omega model's sensitivity to inlet free-stream turbulence from affecting the results of the CFD simulation. Moreover, the SST k-omega model shows good performance in modelling flows with separation flow and adverse pressure gradient.

For turbulent kinetic energy k and specific rate of dissipation ω, the advection-diffusion equations are the following (Qu et al.):

$$\frac{\partial(\rho k)}{\partial t} + \frac{\partial(\rho u_i k)}{\partial x_i} = \frac{\partial}{\partial x_i}\left[(\mu + \sigma_k\mu_t)\frac{\partial k}{\partial x_i}\right] + P_k - \beta^*\rho\omega k$$

$$\frac{\partial(\rho\omega)}{\partial t} + \frac{\partial(\rho u_i \omega)}{\partial x_i} = \frac{\partial}{\partial x_i}\left[(\mu + \sigma_\omega\mu_t)\frac{\partial \omega}{\partial x_i}\right] + \alpha\rho S^2 - \beta\rho\omega^2 + 2(1 - F_1)\frac{\rho\sigma_{\omega 2}}{\omega}\frac{\partial k}{\partial x_i}\frac{\partial \omega}{\partial x_i}$$

Where F_1 (Blending function) is the following function (Qu et al.):

$$F_1 = \tanh\left\{\left\{\min\left[\max\left(\frac{\sqrt{k}}{\beta^* \omega y}, \frac{500v}{y^2 \omega}\right), \frac{4\rho\sigma_{\omega 2} k}{CD_{k\omega} y^2}\right]\right\}^4\right\}$$

$$CD_{k\omega} = \max\left(2\frac{\rho\sigma_{\omega 2}}{\omega}\frac{\partial k}{\partial x_i}\frac{\partial \omega}{\partial x_i}, 10^{-10}\right)$$

y represents the closest distance to a wall. μ_t, which represents the dynamic viscosity, is modelled using the following equation:

$$\mu_t = \frac{\rho a_1 k}{\max(a_1 \omega, SF_2)}$$

Where the invariant measure of the strain rate S is calculated using the following equation:

$$S = \sqrt{2S_{ij}S_{ij}}$$

Meanwhile, F_2, the second blending function, is the following function (Qu et al.):

$$F_2 = \tanh\left[\left[\max\left(\frac{2\sqrt{k}}{\beta^* \omega y}, \frac{500v}{y^2 \omega}\right)\right]^2\right]$$

For the following production term P_k

$$P_k = \min(G, 10\beta^* \rho \omega k)$$

G is given by the following equation:

$$G = \mu_t \frac{\partial u_i}{\partial x_j}\left(\frac{\partial u_i}{\partial x_j} + \frac{\partial u_j}{\partial x_i}\right)$$

The equation below blends the constants $\alpha_k, \alpha_\omega, \alpha$ and β.

$$\phi = F_1 \phi_1 + (1 - F_1)\phi_2$$

For the SST k-omega turbulence model, the following constants are used:

$\beta^* = 0.09$

$\alpha_1 = 5/9$

$\beta_1 = 0.075$

$\sigma_{k1} = 0.85$

$\sigma_{\omega 1} = 0.5$

$\alpha_2 = 0.44$

$\beta_2 = 0.0828$

$\sigma_{k2} = 1$

$\sigma_{\omega 2} = 0.856$

3. Aerodynamic Analysis of the Support and Propulsion Systems Based on CFD Simulations

3.1 Setup of the 3D Model

The 3D model of the support and propulsion systems were first created in SolidWorks 2021[17]. This included the models of the individual components, such as the rotor blades, the motor casings, the bottom plate, the support rack for the motor, the car

body and the bottom plate. The interior features were not modelled, as only the exterior features were being tested for CFD analysis. All of the models were drawn to a 1:1 scale as a real-life flying vehicle.

The individual components were then exported and assembled into one model using SolidWorks Assembly. The full model for the flying car is shown in the figure below. However, within the testing and simulation process, only the propulsion (blades, motor and motor racks) and support structures (landing gear and bottom plate) were assembled and tested due to restrictions in computing prowess as shown in figure 3.1.

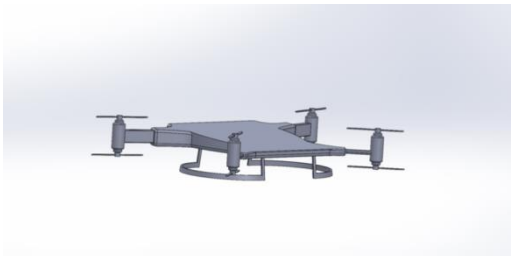

Figure 3.1 3D model of the support and propulsion systems

Before the meshing process begins, the assembled model was imported into ANSYS SpaceClaim, where it was set up to be viable for testing in ANSYS Fluent. First, an enclosure was generated around the model using the enclosure tool. The enclosure acts like a wind tunnel that the car is tested in as shown in figure 3.2.

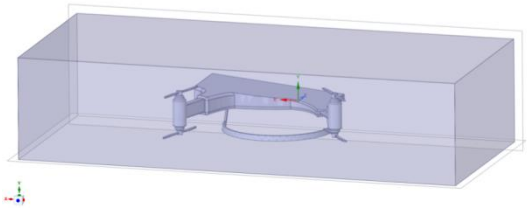

Figure 3.2 The support and propulsion system inside an enclosure

After the enclosure was created, two bodies of influence were added to the model, being the near-field body of influence and the far-field body of influence. Then, the enclosure and the mode were cut with the split body tool. The split body tool could be used in this scenario as the models that are being tested in this research paper are symmetrical along the XY plane. Cutting the enclosure and the model could save computational cost and time as shown in figure 3.3.

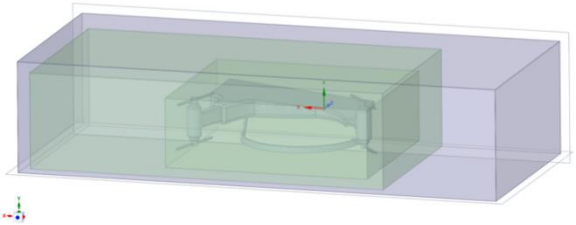

Figure 3.3 The support and propulsion systems inside the two bodies of influence

Before the meshing process, different parts of the model were labelled with their specific names. For example, the front of the enclosure was labeled as inlet, and the back of the enclosure was labeled as outlet. Overall, the inlet and the outlet, the near

field and far field bodies of influence, the individual parts of the support and propulsion structures, the symmetry and the tunnel walls were all labelled. The final product of this process is ready for meshing using ANSYS Fluent Meshing.

3.2 Mesh

Meshing creates tiny sub-volumes within the created control volume before. The equations of fluid dynamics would then be solved within every small sub-volume to simulate the behavior of the fluid in the small sub-volumes. Then, the behaviors in every small sub-volume would be combined to simulate the fluid flow behavior around the whole model. There are three steps to creating a complete mesh: creating a surface mesh, creating a boundary layer mesh, and creating a volume mesh.

To create a surface mesh, the watertight geometry workflow was first selected. Then, the model was imported into ANSYS Fluent Meshing. After that, local sizing was added to the bodies of influence in the configuration below. Adding local sizing can better help the mesh to be refined and capture the characteristics of fluid flow. Insert image. After adding local sizing, a surface mesh was generated with the following minimum and maximum sizes. The end results yielded a quality of 0.65. This was adequate for CFD analysis.

Next, the different boundaries were described. Most notably, the inlet was set as velocity inlet and outlet was set as pressure outlet. The symmetry was specified as well as the walls. Every part of the model was set as a wall. The entire enclosure was then set as a fluid region. Boundary layers were then added using the smooth transition method with 3 layers. Lastly, the prism mesh was generated using the poly hexacore model with a max cell length of 175mm as shown in figure 3.4. This yielded a volume mesh that had a quality of 0.10, which was adequate for CFD analysis.

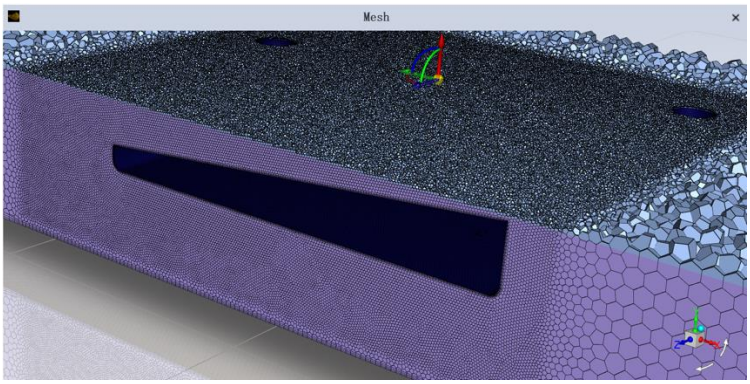

Figure 3.4 Original volume mesh

3.3 Setup of the Solver

The physical conditions of the atmosphere at which the flying car is expected to operate similar to those of air near the ground level. The theoretical flying car that is being tested in this CFD analysis is not expected to fly above an altitude of 1000m above sea level, and it is mostly expected to operate within 250 to 750 meters above sea levels.

Thus, the following constants were used for the air within the CFD analysis as shown in figure 3.5:

Density of the air =1.225 kg/m3

Viscosity of the air =1.7894.

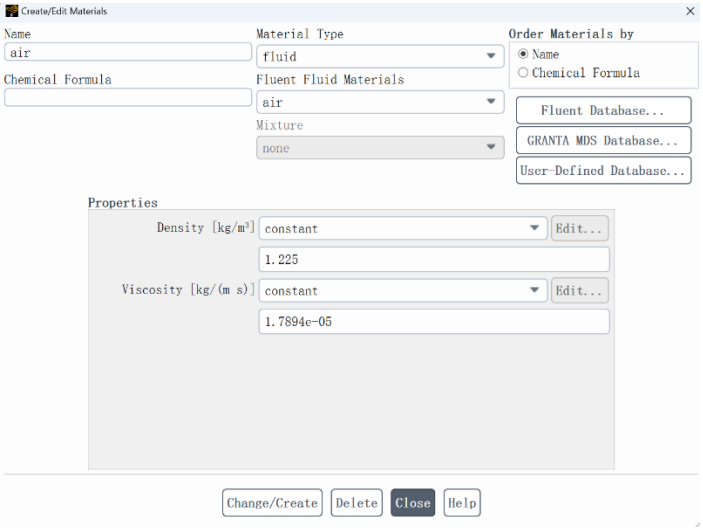

Figure 3.5 The material settings for air

For this simulation, a steady-state calculation was selected. For the boundary conditions, only the setting for the inlet was modified. The interior was kept as the fluid region, while all the tunnel walls and the model being labelled as walls. The outlet was set as a pressure outlet, and the inlet was kept as a velocity inlet. The turbulence was defined using the intensity and viscosity ration method, where the intensity and viscosity ratio were kept at 5% and 10 respectively. While the velocity specification method was set to magnitude and normal to boundary, with the velocity magnitude being 15m/s, 30m/s and 45m/s for each of the trials. The varying velocity simulates the different environments that the flying car might work in, including low speeds (15m/s), medium speeds (30m/s) and high-speed cruising (45m/s). These are also speeds that can be commonly seen on cars in the status quo in cities.

For the viscous flow model, the SST k-omega model was chosen, [18] while all of the other models were turned off as shown in figure 3.6. A report was defined to output the drag force on the model, directly parallel to the direction of the fluid flow. Before the simulation, automatic hybrid initialization was used to initialize the simulation. Lastly, 500 iterations were chosen as the maximum number of iterations.

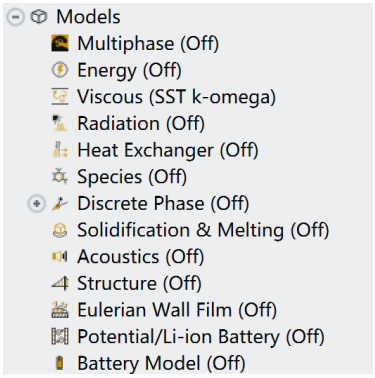

Figure 3.6 The chosen solver models

3.4 Results

For the original support and propulsion structures, the following results were obtained for the frontal drag at different flow velocities.

For an incoming airflow of 15 m/s, the propulsion and support structures had a drag force of 111.68 Newtons, which was a

result that was gained from a convergence after 85 iterations as shown in the following figure.

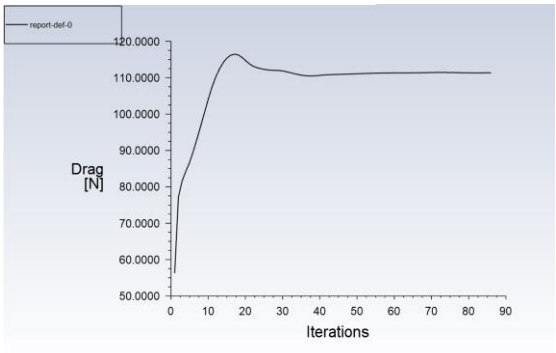

Figure 3.7 The results for 15m/s

For an incoming airflow of 30 m/s, the propulsion and support structures had a drag force of 448.22 Newtons, which was a result gained after a convergence after 95 iterations, as shown in the following figure.

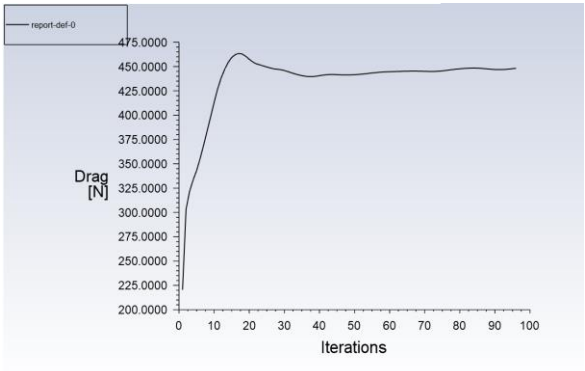

Figure 3.8 The results for 30 m/s

Lastly, for an incoming airflow of 45 m/s, the propulsion and support structures had a drag force of 1041.27 Newtons, which was a result gained after a convergence after 224 iterations, as shown in the following figure.

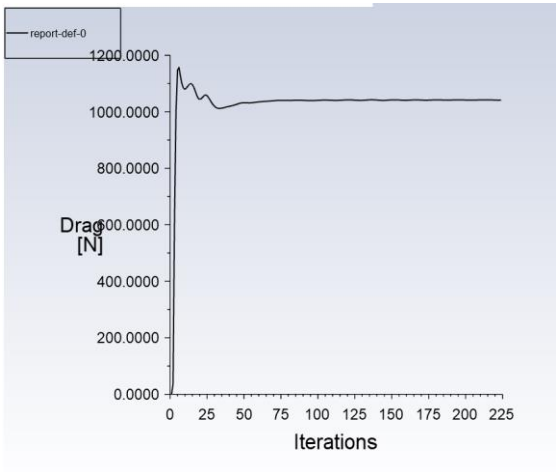

Figure 3.9 The results for 45 m/s

By plotting the three velocities along with the respective drag on the same graph, a quadratic relationship could be seen between the drag and the velocity. This fits the relationship between flow velocity and drag in turbulent flow, where drag is directly

proportional to the square of the incoming flow velocity.

4. Optimization of the External Structure Based on CFD Simulations

4.1 Analysis of the Results of the Simulation

Based on the pressure contour images for the original external structure, the most significant sources of drag could be identified using the areas on the structure that was marked as the most red[19].

For example, in all the pressure contour images for the original external structure, both motors had extremely high-pressure zones where it directly came in contact with the incoming airflow as shown in figure 4.1.

Moreover, the disturbed and turbulent airflow that passed over the first motor rack will directly impact the second motor rack and the second motor, which will cause even more extra drag as airflow passes over the second motor.

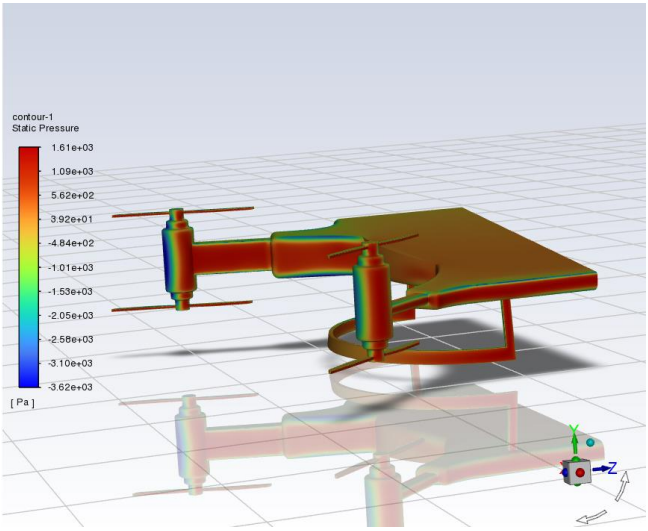

Figure 4.1 Pressure contour for the original system at 45m/s

Overall, the extra frontal area created by separating the two motors and having two separate motor racks means that the incoming airflow will affect a larger area, which contributes to the increasing drag. Moreover, by having the motor racks in a largely rectangular shape, it disturbs the incoming airflow and creates turbulent flow behind it. The turbulent flow will greatly increase drag as opposed to laminar flow.

4.2 Optimization of the Model

The optimization of the support and propulsion structures for the flying car will focus on the following three principles:

a.Reduce frontal area to reduce the area where incoming flow creates drag.

b.Reduce distance between the two motors to prevent turbulent flow from the frontal motor from greatly affecting the rear one.

c.Reduce drag of the supporting structure for the motors themselves.

To follow all the principles at the same time, the was decided that the individual motor racks would be removed, to be replaced by an airfoil that had both motors attached to it as shown in figure 4.2. By replacing individual motor racks with an airfoil, it reduces the drag of the supporting structure through making it aerodynamically optimized. Furthermore, by attaching both the frontal and the rear motor to the same airfoil, it greatly decreased the distance between the two motors, which minimizes the effect of the turbulent flow from the frontal motor on the rear motor. Lastly, by switching to an airfoil as the motors' support

structure, it reduces the frontal area of the car, as it eliminates the need for two separate motor racks, thus decreasing frontal surface area.

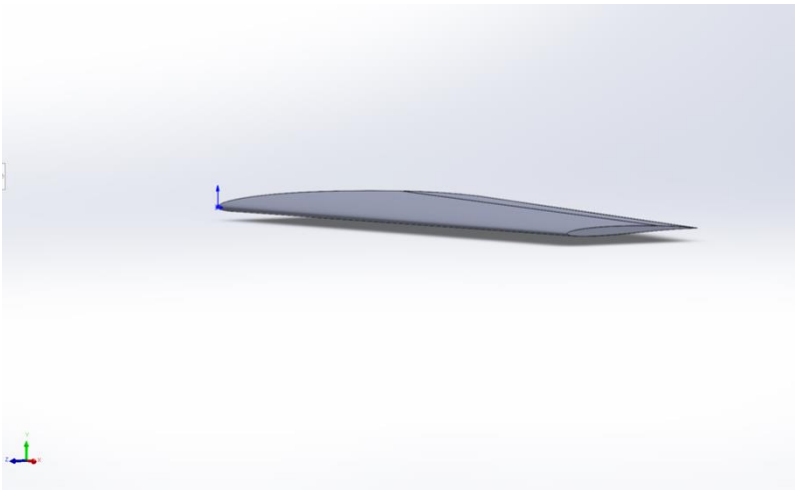

Figure 4.2 Chosen airfoil to replace individual motor racks

4.3 Construction and Meshing of the Optimized Model

The 3D model for the optimized model was constructed on the basis of the original model. The bottom plate was modified to no longer have the individual motor racks, but instead a NACA 4 series airfoil to support the motors. The individual parts were first drawn in SolidWorks 2021, and then assembled as a SolidWorks Assembly as shown in figure 4.3.

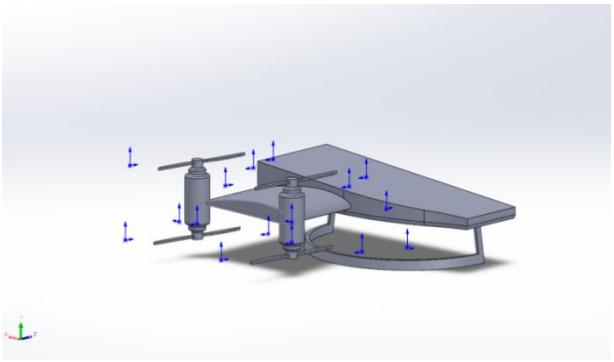

Figure 4.3 3D model of the optimized structure

Then, the 3D model was inserted into ANSYS SpaceClaim, where it was first adjusted to face the right direction on the Cartesian axes. Then, an enclosure was added using the enclosure tool, with the near field and far field bodies of influence being added later using the box tools. Then, the split body tool was used to create the symmetry and reduce computational costs and time. Lastly, the different parts of the model were labelled before meshing.

To create the mesh for the optimized model, the watertight geometry workflow was selected, and then the optimized model was imported into ANSYS Fluent Meshing, where local sizing was added to the different bodies of influence to best simulate for the fluid behavior. After a surface mesh was created, boundaries were specified, and 3 boundary layers were added. Lastly, a volume mesh was created with a maximum cell length of 175mm.

4.4 Results

The same solver setup and number of iterations were chosen for this simulation, and the following results were obtained for the

optimized structure.

For an incoming airflow of 15 m/s, the optimized propulsion and support structures had a drag force of 83.36 Newtons, which was a result that was gained from a convergence after 97 iterations as shown in the following figure.

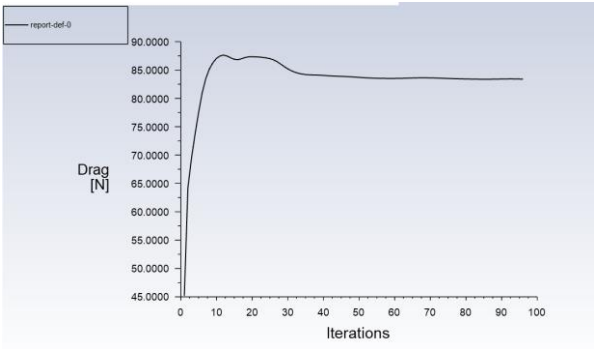

Figure 4.4 The results for 15m/s

For an incoming airflow of 30 m/s, the optimized propulsion and support structures had a drag force of 333.26 Newtons, which was a result gained after a convergence after 95 iterations, as shown in the following graph.

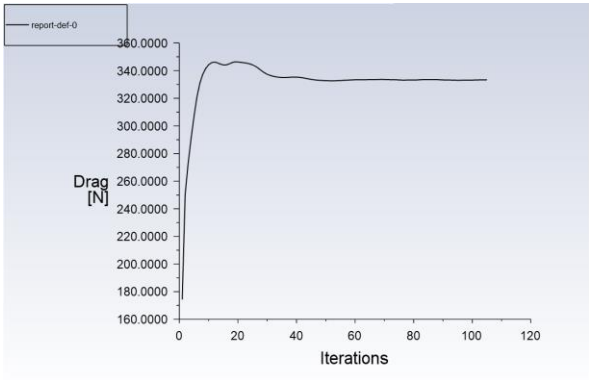

Figure 4.5 The results for 30m/s

Lastly, for an incoming airflow of 45 m/s, the optimized propulsion and support structures had a drag force of 752.87 Newtons, which was a result gained after a convergence after 224 iterations, as shown in the following graph.

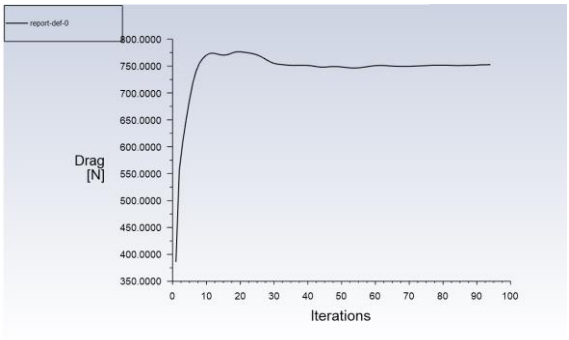

Figure 4.6 The results for 45m/s

After optimizing the external structure of the support and propulsion system, the drag was significantly reduced. For a low velocity of 15m/s, the drag was reduced by 25.4%. For a medium velocity of 30m/s, the drag was reduced by 25.6%. For a relatively high velocity of 45m/s, the drag was reduced by 27.7%. The simulations at three different velocities all suggested a

reduction of drag of over 25% with the optimized structure in place.

Moreover, by analyzing the pressure contours of both models at all velocities, a clear decrease in the area with high pressures could be found (marked as red). The decrease in areas with high pressure indicates a decrease in overall drag, as areas with high fluid pressure represents areas with high drag as shown in figures 4.7 and 4.8.

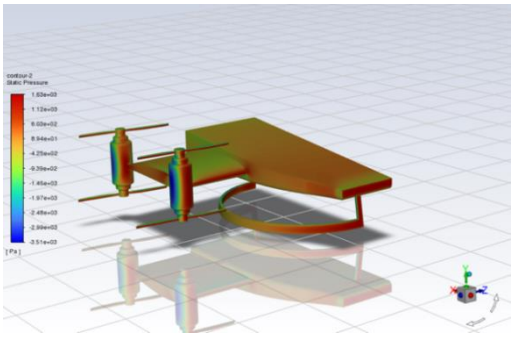

Figure 4.7 Pressure contour for the optimized model at 45m/s

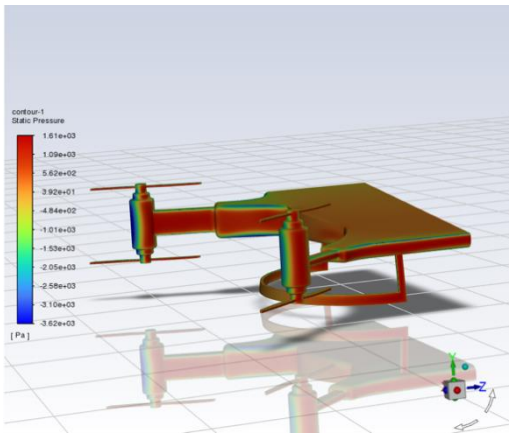

Figure 4.8 Pressure contour for the original structure at 45m/s

5. Conclusion

In this paper, Computational Fluid Dynamics (CFD) simulations were utilized to conduct an aerodynamic optimization of the support and propulsion systems for flying cars. The findings demonstrate that the aerodynamic refinements have significantly reduced the drag experienced by the flying cars at various incoming airflow velocities, thereby effectively enhancing their aerodynamic performance and potential operational efficiency. This study confirms the critical role of CFD simulations in the design and performance improvement of flying cars.

References

[1] US Motor Vehicles Sales Growth,1977–2024|CEIC Data. Accessed 1 Aug. 2024.

[2] GHO|ByCategory|Registered Vehicles-Data by Country. A995. Accessed 1 Aug. 2024.

[3] Anderson, Jr, John D. A History of Aerodynamics: And Its Impact on Flying Machines. Cambridge: Cambridge University Press, 1997. Print. Cambridge Aerospace Series.

[4] Glazener, Andrew, et al. “The Impacts of Car-Free Days and Events on the Environment and Human Health.” Current Environmental Health Reports, vol. 9, no. 2, 2022, pp. 165–82. PubMed Central, https://doi.org/10.1007/s40572-022-

00342-y.

[5] Global Greenhouse Gas Overview | US EPA. Accessed 1 Aug. 2024.

[6] Pan, Gaofeng, and Mohamed-Slim Alouini. "Flying Car Transportation System: Advances, Techniques, and Challenges." IEEE Access, vol. PP, Feb. 2021, pp. 1–1. ResearchGate, https://doi.org/10.1109/ACCESS.2021.3056798.

[7] Waterman Aerobile | National Air and Space Museum. Accessed 10 Aug. 2024.

[8] September 2020 AOTM | U.S. Army Transportation Museum - Joint Base Langley-Eustis, Virginia. https://transportation.army.mil/museum/AOTM/2020/sep_2020.html. Accessed 10 Aug. 2024.

[9] Anderson, John D. "Flight (Aerodynamics)." Encyclopedia of Physical Science and Technology (Third Edition), edited by Robert A. Meyers, Academic Press, 2003, pp. 1–21. ScienceDirect, https://doi.org/10.1016/B0-12-227410-5/00915-7.

[10] Bendjebbas, H., et al. "Full-Scale, Wind Tunnel and CFD Analysis Methods of Wind Loads on Heliostats: A Review." Renewable and Sustainable Energy Reviews, vol. 54, Feb. 2016, pp. 452–72. ScienceDirect, https://doi.org/10.1016/j.rser.2015.10.031.

[11] Duncan, W. J. "Theoretical Aerodynamics." Nature, vol. 161, no. 4097, May 1948, pp. 703–04. www.nature.com, https://doi.org/10.1038/161703b0.

[12] Niemann, Hans-Jürgen. "The Boundary Layer Wind Tunnel: An Experimental Tool in Building Aerodynamics and Environmental Engineering." Journal of Wind Engineering and Industrial Aerodynamics, vol. 48, no. 2, Oct. 1993, pp. 145–61. ScienceDirect, https://doi.org/10.1016/0167-6105(93)90133-9.

[13] Wu, Jiezhi, et al. "Fundamental Theories of Aerodynamic Force in Viscous and Compressible Complex Flows." Progress in Aerospace Sciences, vol. 99, May 2018, pp. 27–63. ScienceDirect, https://doi.org/10.1016/j.paerosci.2018.04.002.

[14] Introduction to Computational Fluid Dynamics, An: The Finite Volume Method. https://www.pearson.com/en-us/subject-catalog/p/introduction-to-computational-fluid-dynamics-an-the-finite-volume-method/P200000005670/9780131274983. Accessed 6 Aug. 2024.

[15] Sun, Bohua. "Revisiting the Reynolds-Averaged Navier–Stokes Equations." Open Physics, vol. 19, no. 1, Jan. 2021, pp. 853–62. www.degruyter.com, https://doi.org/10.1515/phys-2021-0102.

[16] Patil, Digambar, and Sachin Kadam. "Basics of Computational Fluid Dynamics: An Overview." IOP Conference Series: Earth and Environmental Science, vol. 1130, no. 1, Jan. 2023, p. 012042. Institute of Physics, https://doi.org/10.1088/1755-1315/1130/1/012042.

[17] Genç, M. Serdar, et al. "An Experimental Study on Aerodynamics of NACA2415 Aerofoil at Low Re Numbers." Experimental Thermal and Fluid Science, vol. 39, May 2012, pp. 252–64. ScienceDirect, https://doi.org/10.1016/j.expthermflusci.2012.01.029.

[18] Wilcox, David C. "Formulation of the K-w Turbulence Model Revisited." AIAA Journal, May 2012. world, arc.aiaa.org, https://doi.org/10.2514/1.36541.

[19] Qu, Sen, et al. "An Evaluation of Different RANS Turbulence Models for Simulating Breaking Waves Past a Vertical Cylinder." Ocean Engineering, vol. 234, Aug. 2021, p. 109195. ScienceDirect, https://doi.org/10.1016/j.oceaneng.2021.109195.